nature nanotechnology

ARTICLES

https://doi.org/10.1038/s41565-018-0145-8

Broadband, electrically tunable third-harmonic generation in graphene

Giancarlo Soavi[1]*, Gang Wang[1], Habib Rostami[2], David G. Purdie[1], Domenico De Fazio[1], Teng Ma[1], Birong Luo[1], Junjia Wang[1], Anna K. Ott[1], Duhee Yoon[1], Sean A. Bourelle[1], Jakob E. Muench[1], Ilya Goykhman[1], Stefano Dal Conte[3,4], Michele Celebrano[4], Andrea Tomadin[2], Marco Polini[2], Giulio Cerullo[3,4] and Andrea C. Ferrari[1]*

Optical harmonic generation occurs when high intensity light (>10^{10} W m^{-2}) interacts with a nonlinear material. Electrical control of the nonlinear optical response enables applications such as gate-tunable switches and frequency converters. Graphene displays exceptionally strong light–matter interaction and electrically and broadband tunable third-order nonlinear susceptibility. Here, we show that the third-harmonic generation efficiency in graphene can be increased by almost two orders of magnitude by controlling the Fermi energy and the incident photon energy. This enhancement is due to logarithmic resonances in the imaginary part of the nonlinear conductivity arising from resonant multiphoton transitions. Thanks to the linear dispersion of the massless Dirac fermions, gate controllable third-harmonic enhancement can be achieved over an ultrabroad bandwidth, paving the way for electrically tunable broadband frequency converters for applications in optical communications and signal processing.

The response of a material to an interaction with an optical field can be described by its polarization ($\vec{\mathbf{P}}$) using the following equation[1]:

$$\vec{\mathbf{P}} = \epsilon_0[\chi^{(1)}\cdot\vec{\mathbf{E}} + \chi^{(2)}:\vec{\mathbf{E}}\vec{\mathbf{E}} + \chi^{(3)}:\vec{\mathbf{E}}\vec{\mathbf{E}}\vec{\mathbf{E}} + \cdots] \quad (1)$$

where $\vec{\mathbf{E}}$ is the incident electric field and ϵ_0 is the permittivity of free space. $\chi^{(1)}$ (dimensionless) is the linear susceptibility, while the tensors $\chi^{(2)}$ [m/V] and $\chi^{(3)}$ [m^2/V^2] are the second- and third-order nonlinear susceptibilities. They are often reported in electrostatic units (esu), where the relation between esu and standard units (SI)[2] is $\chi^n(\mathrm{SI})/\chi^n(\mathrm{esu}) = 4\pi/(3\times10^{-4}c)^{n-1}$, with $n = 1,2,3$. Thanks to the nonlinear terms of $\mathbf{P}$, new frequencies can be produced, due to harmonic generation[3] and frequency mixing[4]. For example, in second-harmonic generation (SHG), an incident electromagnetic wave with the angular frequency $\omega_0 = 2\pi\nu$, where ν is the photon frequency, provides via $\chi^{(2)}$ a new electromagnetic wave with angular frequency $2\omega_0$ (ref. [3]). The SHG efficiency (SHGE) is defined as the ratio between the second-harmonic intensity and the intensity of the incoming light. Analogously, third-harmonic generation (THG) is the emission of a photon with energy triple that of the incident one. The THG efficiency (THGE) is defined as the ratio between the third-harmonic intensity and the intensity of the incoming light. Second-order nonlinear processes are also known as three-wave-mixing, as they mix two optical fields to produce a third one[5]. Third-order nonlinear processes are known as four-wave-mixing (FWM)[5], as they mix three fields to produce a fourth one.

Nonlinear optical processes are exploited in a variety of applications, including laser technology[6], material processing[7] and telecommunications[8]. For example, to create new photon frequencies (532 nm from SHG in a neodymium-doped yttrium aluminium garnet (Nd:YAG) laser at 1,064 nm)[9] or broadly tunable ultrashort pulses (femtoseconds to picoseconds) in optical parametric amplifiers (OPAs)[10] and optical parametric oscillators (OPOs)[11]. High harmonic generation is also used for extreme ultraviolet light[12] and attosecond pulse generation[13], while difference frequency generation enables one to create photons in the terahertz range[14]. The ability to cover a large fraction of the electromagnetic spectrum, from ultraviolet to terahertz, is crucial in optical spectroscopy because different energy regions can probe different features of a material. For example, terahertz light can probe vibrational sublevels as well as free electrons in the conduction and valence bands. Visible and near-infrared light can probe interband transitions, mid-infrared light can probe phonons, and ultraviolet light can be used in photoemission spectroscopy for the study of core electronic levels. In telecommunications, frequency conversion for wavelength division multiplexing is based on nonlinear effects, such as FWM[8].

Second-order nonlinear effects can only occur in materials without inversion symmetry, while third-order effects are present in any system independent of symmetry[1]; therefore, they are the main intrinsic nonlinear response for most materials. THG and SHG intensity enhancement was achieved by exploiting magnetic dipole[15] and excitonic resonances[16], surface plasmons in silver films[17], plasmonic nanocavities[18] and photonic-crystal waveguides[19], whereby spatial compression of the optical energy results in an increase of the local optical field. Nonlinear optical effects depend on the characteristics of the impinging light beam (or beams) (that is, frequency, polarization and intensity) and on the properties of the nonlinear material, as dictated by its electronic structure. The ability to electrically control the nonlinear optical response of a material by a gate voltage (V_G) will enable disruptive applications in compact nanophotonic devices with novel functionalities. However, electrical control of the THGE has not yet been reported.

Layered materials have a strong nonlinear optical response[20–27]. Electrically tunable SHG was reported for monolayer WSe_2 for

[1]Cambridge Graphene Centre, University of Cambridge, Cambridge, UK. [2]Istituto Italiano di Tecnologia, Graphene Labs, Genova, Italy. [3]IFN-CNR, Milano, Italy. [4]Dipartimento di Fisica, Politecnico di Milano, Milano, Italy. *e-mail: gs544@cam.ac.uk; acf26@eng.cam.ac.uk

photon energies close to the A exciton (~1.66 eV)[20]. However, the tunability was limited to a narrow band (~10 meV) in the proximity of the excitonic transition. Electrically tunable SHG was also achieved by inversion-symmetry breaking in bilayer MoS_2 close to the C exciton (~2.75 eV)[25], but the SHGE was strongly dependent on the laser detuning with respect to the C exciton transition energy. Thus, in both cases, electrical control was limited to narrow energy bands (~10–100 meV) around the excitonic transitions. Graphene, instead, has electrically tunable nonlinearities over a much broader bandwidth, thanks to the linear dispersion of the Dirac fermions. In single layer graphene (SLG), SHG is forbidden due to symmetry[28–31]. SHG was reported in the presence of an electric current[30,31], but was found to be at least one order of magnitude weaker with respect to third-order nonlinear effects. Thus, third-order nonlinear effects are the most intense terms of the intrinsic nonlinear optical response of SLG.

Third-order nonlinearities in SLG have been studied both theoretically[32–35] and experimentally[21,36,37]. Ref. [21] reported a $1/\omega_0^4$ dependence of the third-order response in a narrow band (emitted photons between ~1.47 and 1.63 eV), but no resonant behaviour or doping dependence. Ref. [37] reported a factor ~2 enhancement in a FWM experiment at the onset of interband transitions ($\hbar\omega_0 = 2|E_F|$, where E_F is the Fermi energy and $\hbar \approx 10^{-34}$ m^2 kg s^{-1} is the reduced Planck constant) for SLG on silicon nitride waveguides in a narrow band (emitted photons between ~0.79 and 0.8 eV). Thus, to date, evidence of tunable third-order nonlinear effects in SLG has been limited to narrow bands and weak enhancements.

Sample preparation and characterization

To test both the photon energy dependence and the electrical tunability of THGE, we use two sets of samples: SLG placed on a transparent substrate (sapphire) (Fig. 1a) and back-gated SLG on a reflective substrate (Si/SiO_2) (Fig. 1b). To study the THGE photon energy dependence, we measure it over a broad range, whereby the incident photon energy is ~0.4–0.7 eV, with a THG signal at ~1.2–2.1 eV, limited by the responsivity of our Si-based charge-coupled device (CCD). Transmission measurements enable us to derive the absolute THGE by taking into account the system losses and by minimizing the chromatic aberrations of the optical components (for example, in reflection, one needs to use beam splitters and these do not have a flat response over the ~0.4–2.2 eV range). Thus, we use chemical vapour deposition (CVD) to obtain large-area SLG (~cm in size) and to simplify the alignment, given the low optical contrast of SLG on sapphire[38]. When measuring the THGE electrical tunability, we need to follow the THG intensity normalized to its minimum, as a function of the gate voltage V_G. For each ω_0 we measure the THG spectra as a function of V_G. For each spectrum, we calculate the total number of counts on the CCD, which is proportional to the number of THG photons, and divide all the spectra by that with the minimum counts. The key here is a precise control of E_F, while any system uncertainties on the absolute THGE are removed by the normalization. Thus, we use an exfoliated SLG back-gated field-effect transistor on Si + 285 nm SiO_2. A sketch of the experimental set-up used for the THG experiments, in transmission and reflection, is shown in Fig. 2.

The two sets of samples are prepared and characterized as described in the Methods. E_F for the CVD SLG on sapphire is ~250 meV, and <100 meV in the exfoliated SLG on Si + 285 nm SiO_2. The defect density, n_D, is ~6×10^{10} cm^{-2} for SLG on sapphire and ~2.4×10^{10} cm^{-2} for SLG on Si/SiO_2. The small variation in defects suggests that the samples are comparable. Also, as discussed later, THGE has a negligible dependence on disorder, impurities and imperfections over a range of values representing the vast majority of SLGs in the literature.

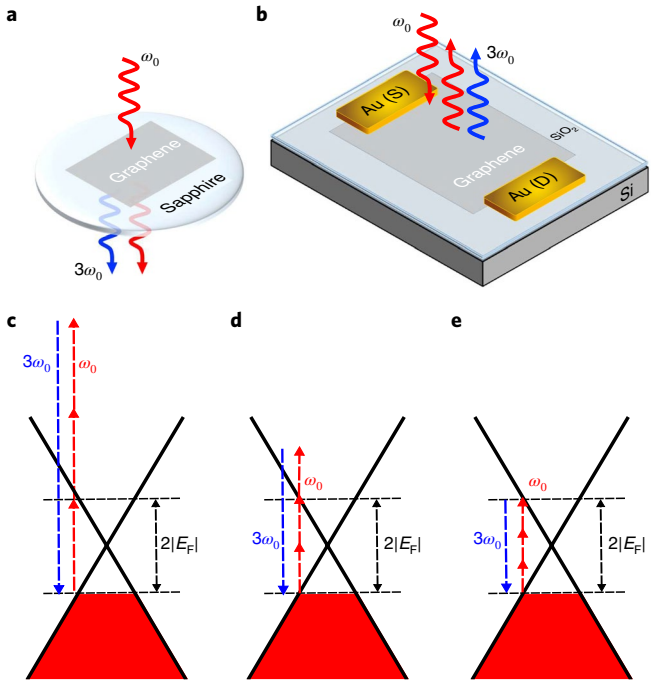

Fig. 1 | THG measurements configurations and multiphoton resonances in SLG. **a**, CVD SLG on sapphire for transmission. **b**, Exfoliated SLG on Si/SiO_2 for reflection, with source (S) and drain (D) gold gates. **c**–**e**, Resonances corresponding to the three logarithmic peaks in the imaginary part of the SLG nonlinear conductivity at $T_e = 0$ K for $\hbar\omega_0 = 2\ |E_F|$ (**c**), $|E_F|$ (**d**), 2/3 $|E_F|$ (**e**). The red arrows represent the incident ω_0 photons and the blue arrows represent the third-harmonic photons at $3\omega_0$. The shaded red areas represent states occupied by electrons.

Photon energy dependence

The THGE measurements are performed in air at room temperature for both transmission and reflection modes. The THG signal is recorded with an iHR550 spectrometer (Horiba) coupled with a CCD detector (Symphony II, Horiba), as detailed in the Methods and in Fig. 2. Figure 3a shows a plot of the representative third-harmonic spectra for different incident $\hbar\omega_0$ for SLG on sapphire (Fig. 1b) after calibration based on the photon energy-dependent losses of the set-up, as described in the Methods. We assign the measured signal to THG because the energy of the detected photons is three times the incident one ($\hbar\omega_{THG} = 3\hbar\omega_0$), and its intensity scales with the cube of the incident power ($I_{3\omega_0} \propto I_{\omega_0}^3$)[1], see also Supplementary Fig. 1. Figure 3b shows that when $\hbar\omega_0$ decreases from ~0.7 to ~0.4 eV, the THGE is enhanced by a factor ~75. This enhancement depends on E_F and the electronic temperature (T_e). In the limit of $E_F = 0$ eV and $T_e = 0$ K the third-order optical conductivity scales as $1/(\hbar\omega_0)^4$ (ref. [33]). In our case, E_F is ~250 meV, and the experiments are performed at room temperature. We explain this enhancement by taking into account the dependence of the third-order optical conductivity $\sigma^{(3)}_{\ell\alpha_1\alpha_2\alpha_3}$, where ℓ and $\alpha_{i=1,2,3}$ are Cartesian indexes, on ω_0, E_F and T_e. Qualitatively, the expected THGE dependence on the incident photon energy and E_F can be understood as follows. The linear optical response of SLG at $T_e = 0$ K has a 'resonance' for $\hbar\omega_0 = 2\ |E_F|$, the onset of intraband and interband transitions[39]. Around this energy, a jump occurs in the real part of $\sigma^{(3)}_{\ell\alpha_1\alpha_2\alpha_3}$, which is due to the relaxation of the Pauli blocking constraint for vertical transitions between massless Dirac bands. From the Kramers–Kronig relations, this jump corresponds to a logarithmic peak in the imaginary part of $\sigma^{(3)}_{\ell\alpha_1\alpha_2\alpha_3}$. In a similar way, for the SLG third-order nonlinear optical response, logarithmic peaks in

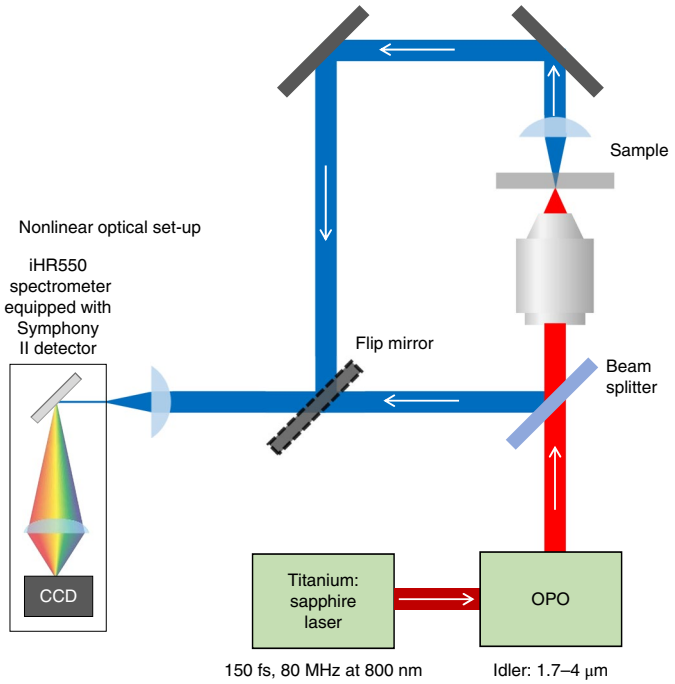

Fig. 2 | Set-up used for the THG experiments. A titanium:sapphire mode-locked laser produces pulses at 800 nm that pump an OPO. For the THG experiments, we used the OPO idler beam, tunable between ~1.7 and 4 μm. This is aligned with a microscope and focused on the sample. The THG signal can be collected either in transmission or reflection with an iHR550 spectrometer coupled with a Symphony II detector (Horiba). A liquid nitrogen-cooled CCD open electrode with 1024×256 pixels is used as the detector. The red lines represent the fundamental beam and the blue lines represent the third-harmonic beam.

the imaginary part of $\sigma^{(3)}_{\ell\alpha_1\alpha_2\alpha_3}$ occur at $T_e=0$ K for multiphoton transitions such that $m\hbar\omega=2\ |E_F|$ with $m=1$, 2, 3, which correspond to incident photon energies $\hbar\omega_0=2\ |E_F|$, $|E_F|$, $2/3\ |E_F|$ (refs [32,33]), as sketched in Fig. 1c–e. At high T_e, due to the broadening of the Fermi–Dirac distribution, these peaks are smeared and merge, as discussed in Supplementary Section 2. A comparison between theoretical curves, for $E_F=250$ meV and different T_e, and experiments is plotted in Fig. 3b. These results indicate that both T_e and E_F play key roles, in particular when $\hbar\omega_0\leq 2|E_F|$. The effects of disorder, impurities and imperfections can be phenomenologically introduced by a relaxation rate, $\Gamma=\hbar/\tau$ (where τ is the scattering time of electrons in SLG), through the density matrix approach[32,34]. Our analysis (see Supplementary Section 2.3 and Supplementary Fig. 4) shows that the effect on THGE of τ in the range ~0.1 fs to $\gg$1 ps is negligible. Thus, we can use ideal SLG in our theory, that is, defect-free, with $\tau\gg 1$ ps, which simplifies the calculations.

Gate tunability

Refs [32,33] predicted that gate tunability of THGE should be possible. Figure 3c plots the THG spectra for different V_G at $\hbar\omega_0=0.59$ eV. Figure 3d shows the THG intensity in the $-600\ \text{meV}\leq E_F\leq+150$ meV range, corresponding to $-150\ \text{V}\leq V_G\leq+150$ V. E_F is derived from each V_G as discussed in the Methods. Figure 3d indicates that, as a function of V_G, there is a THG intensity enhancement by over a factor of 20 starting when $\hbar\omega_0<2\ |E_F|$. The results presented in Fig. 3d also suggest that THGE in SLG follows an opposite trend compared to FWM[37]. That is, it is higher for intraband ($\hbar\omega_0<2\ |E_F|$) than interband ($\hbar\omega_0>2\ |E_F|$) transitions. This result is consistent with the calculations presented in Supplementary Section 2. For both transmission and reflection modes, the THGE for SLG, considered as a nonlinear interface layer between air and substrate, under normal incidence can be written as follows (see Supplementary Section 2.1 and Supplementary Figs. 2 and 3):

$$\eta^{\text{THG}}(\omega_0,E_F,T_e)=\frac{I_{3\omega_0}}{I_{\omega_0}}=f(\omega_0)\frac{I^2_{\omega_0}}{4\epsilon_0^4c^4}\ |\sigma^{(3)}_{\ell\ell\ell\ell}(\omega_0,E_F,T_e)|^2 \qquad (2)$$

where $\epsilon_0\sim 8.85\times10^{-12}$ C(Vm)$^{-1}$ and $c=3\times10^8$ m s^{-1} are the vacuum permittivity and the speed of light, respectively; $f(\omega_0)=n_1^{-3}(\omega_0)n_2(3\omega_0)[n_1(3\omega_0)+n_2(3\omega_0)]^{-2}$ in which $n_{i=1,2}(\omega)$ is the refractive index of air ($i=1$) and substrate ($i=2$). For SLG on any substrate $n_1(\omega)\sim1$ and $n_2(\omega)=\sqrt{\epsilon_2(\omega)}$, with $\epsilon_2(\omega)$ the substrate dielectric function. For sapphire, we use the dispertion relation of the refractive index $n_2(\omega)$. According to the C_{6v} point group symmetry of SLG on a substrate[40], the relative angle between laser polarization and the SLG lattice is not important for the third-order response (see Supplementary Section 2.2). We can therefore assume the incident light polarization $\hat{\ell}$ along the zigzag direction without loss of generality. $\sigma^{(3)}_{\ell\ell\ell\ell}$ can then be calculated employing a diagrammatic technique[24,33,35], where we evaluate a four-leg Feynman diagram for the third-harmonic response function (see Supplementary Section 2 and Supplementary Fig. 2). The light–matter interaction is considered in a scalar potential gauge to capture all intraband, interband and mixed transitions[32–34].

The THGE is proportional to $I^2_{\omega_0}$, as for equation (2). Thus, the THG intensity scales as $I^3_{\omega_0}$ (Supplementary Fig. 11). The $I^2_{\omega_0}$ dependence indicates that the THGE of different experiments should not be directly compared, since differences in average power, spot size, pulse duration, repetition rate, among other factors, will strongly affect its value. As stressed in ref. [36], it is hard to precisely quantify the efficiency of nonlinear effects in SLG. This is because one typically deals with optical powers of the nonlinear signal in the range ~1–100 fW, for which background subtraction becomes critical. The $I^2_{\omega_0}$ dependence makes it even more difficult to estimate the THGE absolute value. The estimate of the losses of the optical set-up also introduces uncertainty. To compare our results with those from the literature, we use $\chi^{(3)}$. There is a large discrepancy in the reported SLG $\chi^{(3)}$, from ~10^{-16} m^2 V^{-2} (ref. [36]) to ~10^{-19} m^2 V^{-2} (ref. [41]). Note that these studies assumed $\chi^{(3)}\equiv i\sigma^{(3)}/(3\epsilon_0\omega_0 d_{\text{eff}})$[34], by considering SLG with a thickness d_{eff}. This approach is incorrect because the effective susceptibilities are well defined only in three-dimensional materials, since they involve a polarization per unit volume[24]. Here, we model directly $\sigma^{(3)}$, therefore we do not need to use d_{eff}. By using the same model as in ref. [36], we obtain $\chi^{(3)}\sim5\times10^{-18}$ m^2 V^{-2} at $\hbar\omega_0\sim0.7$ eV and $\chi^{(3)}\sim8\times10^{-17}$ m^2 V^{-2} at $\hbar\omega_0\sim0.4$ eV for SLG on sapphire ($|E_F|\sim250$ meV). This is one order of magnitude smaller than in ref. [36]. However, $\chi^{(3)}$ in ref. [36] is one to three orders of magnitude larger than any other THG experiments on SLG[24,41], thus not reproducible.

Electronic temperature

Both E_F and T_e play key roles in THGE. The plot in Fig. 3b indicates that T_e is well above room temperature during the THG experiments. The experimental enhancement between 0.69 and 0.41 eV is ~68. From the theoretical curves (dashed lines) in Fig. 3b, the enhancement between 0.69 and 0.41 eV is ~1,400 at $T_e=300$ K, ~180 at 1,000 K, ~65 at 2,000 K and ~50 at 3,000 K. These data indicate that the T_e is in the range 1,000–2,000 K. Figure 4 shows the comparison of experimental and theoretical results for THGE for four $\hbar\omega_0$ between 0.41 and 0.69 eV and different T_e. Each curve, both theoretical (dashed lines) and experimental (open circles), is normalized by its minimum value, to highlight the V_G-dependent enhancement of THGE at different T_e. Both the experimental and theoretical data display a plateau-like feature for THGE at low $|E_F|$ ($2\ |E_F|<\hbar\omega_0$), which corresponds to interband transitions.

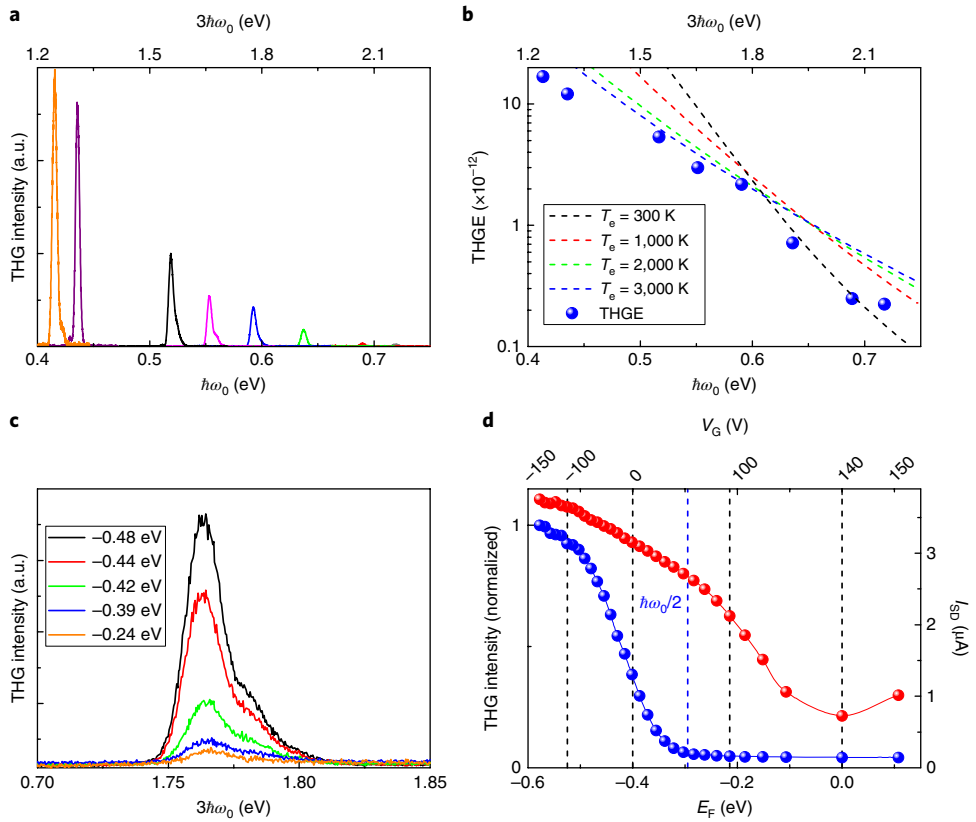

Fig. 3 | Energy dependence and gate tunability of THG. **a**, THG spectra for SLG on sapphire (Fig. 1b) for $\hbar\omega_0$ ~0.4 to ~0.7 eV and an average incident power ~1 mW. The different coloured curves represent theoretical calculations for different T_e. **b**, THGE for SLG on sapphire (Fig. 1b) as a function of $\hbar\omega_0$ (bottom *x* axis) and $3\hbar\omega_0$ (top *x* axis). Curves are calculated for $\tau \gg 1$ps and increasing T_e for $E_F = 250$ meV and $I_{\omega_0} \sim 2.4 \times 10^{12}$ W m^{-2}. The coloured dotted lines are theoretical curves while blue circles are experimental data. **c**, THG spectra as a function of E_F for exfoliated SLG on Si/SiO_2 (Fig. 1c) for $\hbar\omega_0 = 0.59$ eV. **d**, THG intensity (left *y* axis, blue filled circles) and source–drain current (I_{SD}) (right *y* axis, red filled circles) as a function of E_F (bottom *x* axis) and corresponding V_G (top *x* axis) for SLG on Si/SiO_2 (Fig. 1c).

By further increasing $|E_F|$, we reach the energy region for intraband transitions ($\hbar\omega_0 < 2\ |E_F|$), where we observe a THGE rise of up to a maximum for $|E_F| \sim 1.25\hbar\omega_0$ (Fig. 4a). This effect is due to the merging of the two $T_e = 0$ K resonances at $|E_F|\ /\hbar\omega_0 = 1$ and 1.5 as a result of high T_e (see Supplementary Section 2.4 and Supplementary Figs. 5 and 6). Figure 4 indicates that the best agreement between theory and experiments is reached when ~1,000 K $\leq T_e \leq$ 2,000 K, consistent with Fig. 3b. The data for all incident photon energies are well reproduced by the theoretical curves at $T_e = 2{,}000$ K for $|E_F| < \hbar\omega_0 / 2$. For $|E_F| > \hbar\omega_0 / 2$, the data are better reproduced by theoretical curves with lower T_e ~1,000–1,500 K. This can be understood by taking into account the dependence of the linear absorption of SLG on $\hbar\omega_0$, E_F and T_e, as discussed in the Supplementary Sections 3 and 4. For finite T_e (>300 K), interband transitions can also occur for $\hbar\omega_0 < 2|E_F|$ due to thermal broadening of the SLG Fermi–Dirac distribution (see Supplementary Section 4.1). Intraband transitions also contribute to an increase of T_e, especially when $\hbar\omega_0$ is $<2|E_F|$.

T_e can also be estimated as follows. When a pulse of duration Δt and fluence $\mathcal{F}$, with average absorbed power per unit area P/A, photoexcites SLG, the variation dU of the energy density in a time interval dt is dU = (P/A)dt. The corresponding T_e increase is $dT_e = dU/c_v$, where c_v is the electronic heat capacity of the photoexcited SLG, as derived in Supplementary Section 3 and Supplementary Figs. 7 and 8. When the pulse is off, T_e relaxes towards the lattice temperature on a time scale τ. This effect reduces T_e by $dT_e = -(T_e/\tau)$dt in a time interval dt. Thus, we can write the following equation:

$$\frac{dT_e}{dt} = \frac{\alpha}{c_v}\frac{\mathcal{F}}{\Delta t} - \frac{T_e - T_0}{\tau} \tag{3}$$

where T_0 is the initial temperature, and alpha is the SLG absorption. If the pulse duration is (1) much longer than ~20 fs, which is the time scale for the electron distribution to relax to the Fermi–Dirac profile in both bands[42,43], and (2) comparable to the time scale ~150–200 fs needed to heat the optical phonon modes[42–45], T_e reaches a steady-state during the pulse, given by the following equation:

$$T_e = T_0 + \tau\frac{\alpha}{c_v(\mu_c, \mu_v, T_e)}\frac{\mathcal{F}}{\Delta t}. \tag{4}$$

where μ_c and μ_v are the valence and conduction band chemical potentials α and the T_e dependence of c_v in equation (4) are described in Supplementary Sections 3 and 4. In our experiments, $\mathcal{F} \approx 70\,\mu$J cm^{-2} and $\Delta t \approx 300$ fs. Based on this model, T_e is ~1,000–1,500 K for $|E_F| < \hbar\omega_0 / 2$ and ~500 K for $E_F \gg \hbar\omega_0 / 2$, if the residual intraband absorption is 0.1%, as shown in Supplementary Section 4.2 and Supplementary Figs. 9–11. This is in good agreement with the THGE shown in Fig. 4, where we see a reduction of 25–50% of the T_e at $|E_F| = \hbar\omega_0 / 2$. This confirms the trend of THGE as a function of T_e.

Conclusions

The THGE in SLG can be modulated by over one order of magnitude by controlling its E_F and by almost two orders of magnitude

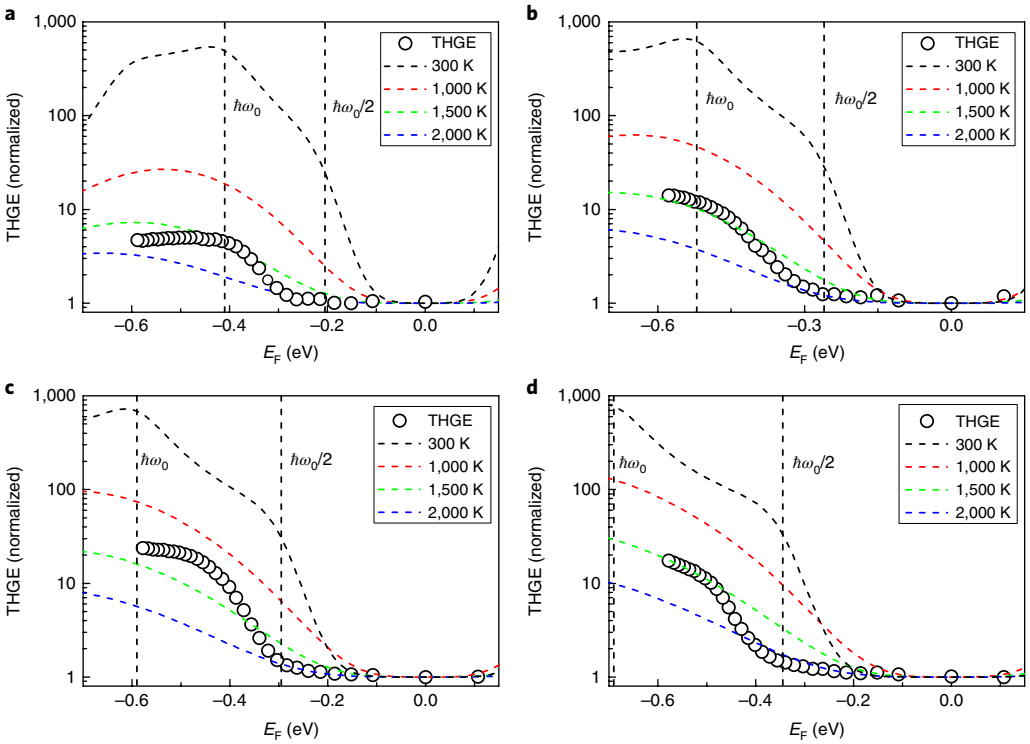

Fig. 4 | Broadband THGE electrical modulation. **a**–**d**, Experimental (open circles) and theoretical (broken lines) data for THGE as a function of E_F, T_e for SLG on Si/SiO_2 at incident photon energies of 0.41 (**a**), 0.52 (**b**), 0.59 (**c**) and 0.69 eV (**d**). The vertical dotted lines in each panel are at $|E_F| = \hbar\omega_0/2$ and $\hbar\omega_0$.

by tuning the incident photon energy in the range ~0.4–0.7 eV. The observation of a steep increase of THGE at $|E_F| = \hbar\omega_0/2$ for all the investigated photon energies suggests that the effect can be observed over the entire linear bandwidth of the SLG massless Dirac fermions. This paves the way for novel SLG-based nonlinear photonic devices, in which the gate tunability of THG may be exploited to implement on-chip schemes for optical communications and signal processing, such as ultra-broadband frequency converters.

Methods

Methods, including statements of data availability and any associated accession codes and references, are available at https://doi.org/10.1038/s41565-018-0145-8.

Received: 14 October 2017; Accepted: 11 April 2018;
Published online: 21 May 2018

References

1. Shen, Y. R. *The Principles of Nonlinear Optics* (John Wiley & Sons, NY, 1984).
2. Butcher, P. N. & Cotter, D. *The Elements of Nonlinear Optics* (Cambridge University Press, Cambridge, 1991).
3. Franken, P. A., Hill, A. E., Peters, C. W. & Weinreich, G. Generation of optical harmonics. *Phys. Rev. Lett.* **7**, 118–119 (1961).
4. Stolen, R. H., Bjorkholm, J. E. & Ashkin, A. Phase-matched three-wave mixing in silica fiber optical waveguides. *Appl. Phys. Lett.* **24**, 308 (1974).
5. Armstrong, J. A., Bloembergen, N., Ducuing, J. & Pershan, P. S. Interactions between light waves in a nonlinear dielectric. *Phys. Rev.* **127**, 1918 (1962).
6. Steinmeyer, G., Sutter, D. H., Gallmann, L., Matuschek, N. & Keller, U. Frontiers in ultrashort pulse generation: pushing the limits in linear and nonlinear optics. *Science* **286**, 1507–1512 (1999).
7. Chang, J. J., Warner, B. E., Dragon, E. P. & Martinez, M. W. Precision micromachining with pulsed green lasers. *J. Laser Appl.* **10**, 285 (1998).
8. Garmire, E. Nonlinear optics in daily life. *Opt. Express* **21**, 30532–30544 (2013).
9. Miller, G. D. et al. 42%-efficient single-pass cw second-harmonic generation in periodically poled lithium niobate. *Opt. Lett.* **22**, 1834–1836 (1997).
10. Cerullo, G. & De Silvestri, S. Ultrafast optical parametric amplifiers. *Rev. Sci. Instrum.* **74**, 1 (2003).
11. Bosenberg, W. R., Drobshoff, A., Alexander, J. I., Myers, L. E. & Byer, R. L. 93% pump depletion, 3.5-W continuous-wave, singly resonant optical parametric oscillator. *Opt. Lett.* **21**, 1336–1338 (1996).
12. Corkum, P. B. Plasma perspective on strong field multiphoton ionization. *Phys. Rev. Lett.* **71**, 1994–1997 (1993).
13. Corkum, P. B. & Krausz, F. Attosecond science. *Nat. Phys.* **3**, 381–387 (2007).
14. Ferguson, B. & Zhang, X.-C. Materials for terahertz science and technology. *Nat. Mater.* **1**, 26–33 (2002).
15. Shcherbakov, M. R. et al. Enhanced third-harmonic generation in silicon nanoparticles driven by magnetic response. *Nano. Lett.* **14**, 6488–6492 (2014).
16. Chen, R., Lin, D. L. & Mendoza, B. Enhancement of the third-order nonlinear optical susceptibility in Si quantum wires. *Phys. Rev. B* **48**, 11879–11882 (1993).
17. Tsang, T. Y. F. Surface-plasmon-enhanced third-harmonic generation in thin silver films. *Opt. Lett.* **21**, 245–247 (1996).
18. Cai, W., Vasudev, A. P. & Brongersma, M. L. Electrically controlled nonlinear generation of light with plasmonics. *Science* **6050**, 1720–1723 (2011).
19. Corcoran, B. et al. Green light emission in silicon through slow-light enhanced third-harmonic generation in photonic-crystal waveguides. *Nat. Photon.* **3**, 206–210 (2009).
20. Seyler, K. L. et al. Electrical control of second-harmonic generation in a WSe_2 monolayer transistor. *Nat. Nanotech.* **10**, 407–411 (2015).
21. Hendry, E., Hale, P. J., Moger, J., Savchenko, A. K. & Mikhailov, S. A. Coherent nonlinear optical response of graphene. *Phys. Rev. Lett.* **105**, 097401 (2010).
22. Wang, G. et al. Giant enhancement of the optical second-harmonic emission of WSe_2 monolayers by laser excitation at exciton resonances. *Phys. Rev. Lett.* **114**, 097403 (2015).
23. Liu, H. et al. High-harmonic generation from an atomically thin semiconductor. *Nat. Phys.* **13**, 262–265 (2017).
24. Saynatjoki, A. et al. Ultra-strong nonlinear optical processes and trigonal warping in MoS_2 layers. *Nat. Commun.* **8**, 893 (2017).
25. Klein, J. et al. Electric-field switchable second-harmonic generation in bilayer MoS_2 by inversion symmetry breaking. *Nano. Lett.* **17**, 392–398 (2017).
26. Sun, Z. et al. Graphene mode-locked ultrafast laser. *ACS Nano* **4**, 803–810 (2010).
27. Bonaccorso, F., Sun, Z., Hasan, T. & Ferrari, A. C. Graphene photonics and optoelectronics. *Nat. Photon.* **4**, 611–622 (2010).

28. Mikhailov, S. A. Theory of the giant plasmon-enhanced second-harmonic generation in graphene and semiconductor two-dimensional electron systems. *Phys. Rev. B* **84**, 045432 (2011).
29. Dean, J. J. & van Driel, H. M. Graphene and few-layer graphite probed by second-harmonic generation: theory and experiment. *Phys. Rev. B* **82**, 125411 (2010).
30. An, Y. Q., Nelson, F., Lee, J. U. & Diebold, A. C. Enhanced optical second-harmonic generation from the current-biased graphene/SiO_2/Si(001) structure. *Nano. Lett.* **13**, 2104–2109 (2013).
31. An, Y. Q., Rowe, J. E., Dougherty, D. B., Lee, J. U. & Diebold, A. C. Optical second-harmonic generation induced by electric current in graphene on Si and SiC substrates. *Phys. Rev. B* **89**, 115310 (2014).
32. Mikhailov, S. A. Quantum theory of the third-order nonlinear electrodynamic effects of graphene. *Phys. Rev. B* **93**, 085403 (2016).
33. Rostami, H. & Polini, M. Theory of third-harmonic generation in graphene: a diagrammatic approach. *Phys. Rev. B* **93**, 161411 (2016).
34. Cheng, J. L., Vermeulen, N. & Sipe, J. E. Third order optical nonlinearity of graphene. *N. J. Phys.* **16**, 053014 (2014).
35. Rostami, H., Katsnelson, M. I. & Polini, M. Theory of plasmonic effects in nonlinear optics: the case of graphene. *Phys. Rev. B* **95**, 035416 (2017).
36. Kumar, N. et al. Third harmonic generation in graphene and few-layer graphite films. *Phys. Rev. B* **87**, 121406(R) (2013).
37. Alexander, K., Savostianova, N. A., Mikhailov, S. A., Kuyken, B. & Van Thourhout, D. Electrically tunable optical nonlinearities in graphene-covered SiN waveguides characterized by four-wave mixing. *ACS Photonics* **4**, 3039–3044 (2017).
38. Casiraghi, C. et al. Rayleigh imaging of graphene and graphene layers. *Nano. Lett.* **7**, 2711–2717 (2007).
39. Mak, K. F. et al. Measurement of the optical conductivity of graphene. *Phys. Rev. Lett.* **101**, 196405 (2008).
40. Mañes, J. L. Symmetry-based approach to electron-phonon interactions in graphene. *Phys. Rev. B* **76**, 045430 (2007).
41. Woodward, R. I. et al. Characterization of the second- and third-order nonlinear optical susceptibilities of monolayer MoS_2 using multiphoton microscopy. *2D Mater.* **4**, 011006 (2017).
42. Brida, D. et al. Ultrafast collinear scattering and carrier multiplication in graphene. *Nat. Commun.* **4**, 1987 (2013).
43. Breusing, M. et al. Ultrafast nonequilibrium carrier dynamics in a single graphene layer. *Phys. Rev. B* **83**, 153410 (2011).
44. Lazzeri, M., Piscanec, S., Mauri, F., Ferrari, A. C. & Robertson, J. Electron transport and hot phonons in carbon nanotubes. *Phys. Rev. Lett.* **95**, 236802 (2005).
45. Piscanec, S., Lazzeri, M., Mauri, F., Ferrari, A. C. & Robertson, J. Kohn anomalies and electron–phonon interactions in graphite. *Phys. Rev. Lett.* **93**, 185503 (2004).

Acknowledgements

We acknowledge funding from EU Graphene Flagship, ERC Grant Hetero2D, and EPSRC grants EP/K01711X/1, EP/K017144/1, EP/N010345/1 and EP/L016087/1.

Author contributions

A.C.F, G.C. and G.S. conceived and designed the experiments. G.S. and G.W. prepared the experimental set-up. G.S., G.W, S.D.C., M.C. and S.A.B. performed the THG experiments. G.S. analysed the THG data. A.K.O. and D.Y. measured the Raman spectra. D.G.P., T.M., B.L., D.D.F., J.W., J.E.M. and I.G. prepared the samples. H.R. and A.T. developed the THG theory and model for T_e. G.S., A.C.F., G.C. and M.P. wrote the paper, with input from all authors.

Competing interests

The authors declare no competing interests.

Additional information

Supplementary information is available for this paper at https://doi.org/10.1038/s41565-018-0145-8.

Reprints and permissions information is available at www.nature.com/reprints.

Correspondence and requests for materials should be addressed to G.S. or A.C.F.

Publisher's note: Springer Nature remains neutral with regard to jurisdictional claims in published maps and institutional affiliations.

Methods

Sample preparation and characterization. SLG on sapphire is prepared as follows. SLG is grown by CVD on copper as previously described[46]. A copper foil (99.8% pure) substrate is placed in a furnace. Annealing is performed at 1,000 °C in a 20 sccm (standard cubic centimetres per minute) hydrogen atmosphere at ~196 mtorr for 30 min. Growth is then initiated by introducing 5 sccm methane for 30 min. The resulting film is characterized by Raman spectroscopy[47,48] using a Horiba Labram HR800 spectrometer equipped with a ×100 objective at 514 nm, with a power on the sample ~500 μW to avoid any possible heating effects. The D to G intensity ratio is I(D)/I(G) ≪ 0.1, corresponding to a defect density $n_D \ll 2.4\times10^{10}\,cm^{-2}$ (refs [49,50]). The 2D peak position (Pos(2D)) and full width at half maximum (FWHM(2D)) are ~2,703 cm^{-1} and ~36 cm^{-1}, while the G peak position (Pos(G)) and FWHM (FWHM(G)) are ~1,585 cm^{-1} and ~18 cm^{-1}. The 2D to G intensity ratio (I(2D)/I(G)) is ~3.3 and the area ratio (A(2D)/A(G)) is ~6.5. The CVD SLG is then transferred onto sapphire by polymer-assisted copper wet etching[51] using polymethyl methacrylate. After transfer, we have Pos(2D) ~2,684 cm^{-1}, FWHM(2D) ~24 cm^{-1}, Pos(G) ~1,584 cm^{-1}, FWHM(G) ~13 cm^{-1}, I(2D)/I(G) ~5.3 and A(2D)/A(G) ~10. From refs [52,53], we estimate E_F as ~250 meV. After transfer, I(D)/I(G) ~0.14, which corresponds to n_D of $\sim6.0\times10^{10}\,cm^{-2}$ (refs [49,50]) with a small increase of defect density.

The back-gated SLG sample is prepared by micromechanical exfoliation of graphite on Si + 285 nm SiO_2 (ref. [54]). Suitable single-layer flakes are identified by optical microscopy[38] and Raman spectroscopy[47,48]. The device is then prepared as follows. We deposit a resist (A4–495) on the exfoliated SLG on Si/SiO_2 and pattern it with electron beam lithography. Then, we develop the resist in a solution of isopropanol diluted with distilled water, evaporate and lift-off 5/70 nm of chromium/gold. Chromium is used to improve the adhesion of gold, while gold is used for source–drain contacts. Raman spectroscopy is then performed after processing. We get Pos(2D) ~2,678 cm^{-1}, FWHM(2D) ~25 cm^{-1}, Pos(G) ~1,581 cm^{-1}, FWHM(G) ~12 cm^{-1}, I(2D)/I(G) ~4.9 and A(2D)/A(G) ~10.3, indicating an E_F <100 meV (refs [52,53]), as well as I(D)/I(G) ≪0.1, corresponding to $n_D \ll 2.4\times10^{10}\,cm^{-2}$ (refs [49,50]).

When V_G is applied, E_F is derived from V_G as follows[52]:

$$E_F = \hbar v_F \sqrt{\pi n} \tag{5}$$

where n is the SLG carrier concentration. This can be written as follows[52]:

$$n = \frac{C_{BG}}{e}(V_G - V_0) \tag{6}$$

where $C_{BG} = \epsilon\epsilon_0/d_{BG} = 1.2\times10^{-8}\,F\,cm^{-2}$ is the back-gate capacitance (d_{BG} = 285 nm is the back-gate thickness and ϵ ~4 is the SiO_2 dielectric constant[52]), $e > 0$ is the fundamental charge and V_0 is the voltage at which the resistance of the SLG back-gated device reaches its maximum (minimum of the current between source and drain). We note that the SLG quantum capacitance (C_{QC}) is negligible in this context. The SiO_2 layer and SLG can be considered as two capacitors in series and the SLG C_{QC} is $\sim10^{-6}\,F\,cm^{-2}$ (ref. [55]). Thus, the total capacitance $C_{total} = (1/C_{BG} + 1/C_{QC})^{-1} \sim C_{BG}$.

THGE measurements and calibration. THGE measurements are performed in air at room temperature for both transmission and reflection modes, as shown in Fig. 2. For excitation we use the idler beam of an OPO (Coherent) tunable between ~0.31 eV (4 μm) and ~0.73 eV (1.7 μm). This is pumped by a mode-locked titanium:sapphire laser (Coherent) with 150 fs pulse duration, 80 MHz repetition rate and 4 W average power at 800 nm. The OPO idler is focused by a × 40 reflective objective (silver coated, numerical aperture of 0.5) to avoid chromatic aberrations. The THG signal is collected by the same objective (in reflection mode) or collimated by an 8 mm lens (in transmission mode) and delivered to a spectrometer (Horiba iHR550) equipped with a nitrogen-cooled Si CCD. The idler spot-size is measured using the razor-blade technique, and is determined to be ~4.7 μm. This corresponds to an excitation fluence ~70 μJ cm^{-2} for the average power (1 mW) used in our experiments. The idler pulse duration is checked by autocorrelation measurements, based on two-photon absorption on a single channel Si photodetector, and is ~300 fs. Under these conditions, the THG signal is stable over at least 1 h. For the V_G-dependent THGE measurements, we use a Keithley 2612B dual channel source meter to apply V_G between −150 and + 150 V, a source–drain voltage (10 mV), as well as to read the source–drain current (I_{SD}). For the photon energy-dependence measurements, we use 60 s acquisition time and 10 accumulations (giving a total of 10 min for each spectrum). For the gate-dependence measurements, we proceed as follows. We tune V_G (62 points between −150 and +150 V) and for each V_G we measure the THG signal by using 10 s of acquisition time and 1 accumulation. We use a shorter accumulation time compared with the photon energy measurements to reduce the total time required for each V_G scan. A lower accumulation time implies that fewer photons are collected by the CCD. We consider the amplitude of THG in counts per s, by dividing the number of counts detected on the CCD by the accumulation time. Thus, in the case of V_G-dependent measurements, SLG is kept at a given V_G for 10 s before moving to the next point (next value of V_G). This corresponds to ~10 min for each measurement (that is, a full V_G scan between −150 and +150 V). In this way, for each V_G and, consequently, for each E_F, we record one THG signal spectrum.

To estimate the ω_0-dependent THGE, it is necessary to first characterize the photon energy-dependent losses of the optical set-up. The pump power is measured on the sample by removing it and measuring the power after the objective. The major losses along the optical path are the absorption of sapphire, the grating efficiency and the CCD quantum efficiency. We also need to consider the CCD gain. The sapphire transmittance is ~85% in the energy range of our THG experiments. To evaluate the losses of the grating and the absorption of the CCD, we align the titanium:sapphire laser, tunable between ~1.2 and 1.9 eV (~650–1,050 nm), with the microscope and detected it on the CCD. We then measure the signal on the spectrometer, given a constant number of photons for all wavelengths, and compare this value with the spectrometer specifications. The spectrometer used in our set-up is a Horiba Symphony II 1,024 × 256 equipped with a Cryogenic Open-Electrode CCD Detector. The quantum efficiency and grating (300 gr mm^{-1}, Blazed 600 nm 510 19 140) relative efficiency are available from the Horiba website (http://www.horiba.com/us/en/scientific/products/optical-spectroscopy/detectors/scientific-cameras-for-spectroscopy-cdd-ingaas-emccd/ccds/details/symphony-ii-ccd-detectors-214/). We obtain an excellent agreement between the two methods (that is, evaluation of the losses from detection of the fundamental beam and spectrometer specifications). Thus, we use the spectrometer specifications to estimate the losses due to grating and CCD efficiencies. We also account for the CCD gain; that is, the number of electrons necessary to have 1 count. The instrument specifications gave a gain of ~7.

Data availability. The data that support the plots within this paper and other findings of this study are available from the corresponding author upon reasonable request.

References

46. Li, X. S. et al. Large-area synthesis of high-quality and uniform graphene films on copper foils. *Science* **324**, 1312–1314 (2009).
47. Ferrari, A. C. & Basko, D. M. Raman spectroscopy as a versatile tool for studying the properties of graphene. *Nat. Nanotech.* **8**, 235–246 (2013).
48. Ferrari, A. C. et al. Raman spectrum of graphene and graphene layers. *Phys. Rev. Lett.* **97**, 187401 (2006).
49. Cancado, L. G. et al. Quantifying defects in graphene via Raman spectroscopy at different excitation energies. *Nano. Lett.* **11**, 3190–3196 (2011).
50. Bruna, M. et al. Doping dependence of the Raman spectrum of defected graphene. *ACS Nano* **8**, 7432–7441 (2014).
51. Bonaccorso, F. et al. Production and processing of graphene and 2D crystals. *Mater. Today* **15**, 564–589 (2012).
52. Das, A. et al. Monitoring dopants by Raman scattering in an electrochemically top-gated graphene transistor. *Nat. Nanotech.* **3**, 210–215 (2008).
53. Basko, D. M., Piscanec, S. & Ferrari, A. C. Electron–electron interactions and doping dependence of the two-phonon Raman intensity in graphene. *Phys. Rev. B* **80**, 165413 (2009).
54. Novoselov, K. S. et al. Two-dimensional atomic crystals. *Proc. Natl Acad. Sci. USA* **102**, 10451–10453 (2005).
55. Xia, J., Chen, F., Li, J. & Tao, N. Measurement of the quantum capacitance of graphene. *Nat. Nanotech.* **4**, 505–509 (2009).